

Published in final edited form as:

Phys Rev B. 2022 February 25; 40(2): . doi:10.1116/6.0001432.

Partial densities of states from x-ray absorption and Auger electron spectroscopy: Use of core-hole memory

Eric L. Shirley^{1,a)}, C. Weiland², J. C. Woicik²

¹Sensor Science Division, Physical Measurement Laboratory, National Institute of Standards and Technology, Gaithersburg, Maryland 20899

²Materials Measurement Science Division, Material Measurement Laboratory, National Institute of Standards and Technology, Gaithersburg, Maryland 20899

Abstract

Ag L_3 edge x-ray absorption and $L_3 - M_{4,5}M_{4,5}$ Auger electron spectra have been measured and simulated for a variety of x-ray electric-field polarization and Auger electron emission directions. The theory relies on density-functional theory, use of the Bethe–Salpeter equation, atomic multiplet theory, and a simplified model for the Auger line shape and its dependence on photon energy. We also demonstrate that partial densities of states for $d T_{2g}$, $d E_g$, and $s A_g$ symmetry partial-wave channels at the Ag site in the solid can be deduced from the experimental measurements with only atomic theoretical input, i.e., with no solid-state theory other than assuming a Fermi edge.

I. INTRODUCTION

Photoemission provides insight about occupied electron states in physical systems, and optical absorption probes excitations that involve a combination of occupied and unoccupied states. However, the relative insensitivity of core electrons to banding effects makes core-excitation spectroscopies uniquely suited for characterizing empty states in a more isolated fashion. While core holes are always created in parallel with photoelectrons in the case of x-ray absorption, the relative simplicity of core-hole states underpins this suitability. Often the energy and polarization dependence of an x-ray absorption spectrum can be almost entirely attributed to aspects of the unoccupied final states, barring energy shifts of spectra from initial-state effects.

For a core level with total angular momentum $j > 1/2$, there is also additional information contained in the core hole's wave function, which remains largely undisturbed provided multipolar interactions between the core hole and the rest of the system can be neglected. This information lies in the form of the components of j , such as j_e , which is the component along an x-ray electric-field polarization direction, \hat{e} . Usually, an absorption experiment senses the cumulative absorbing effect of all electrons in a core subshell (e.g., L_3). The

^{a)}Author to whom correspondence should be addressed: Eric.Shirley@NIST.Gov.

This manuscript is a part of the Special Topic Collection Commemorating the Career of David Arthur Shirley.

content of any “core-hole memory” remains unknown and is eventually lost. This memory is not sophisticated in the sense of being related to a quantum phase, but rather relates to the probability of a core hole having a given value of j_e . Auger decay of core holes is affected by such information, however, so that duly interpreted Auger spectra can provide surprising detail about the empty states into which a photoelectron was initially excited.

In this work, we present results for single-crystal Ag L_3 near-edge x-ray absorption spectroscopy (XAS) and associated $L_3 - M_{4,5}M_{4,5}$ Auger electron spectroscopy (AES). The Auger spectra are reported for the incident x-ray electric-field polarization vector and Auger electrons emitted along the same direction, \hat{e} , which is varied with respect to the sample’s crystallographic axes. In so doing, L_3 electrons with different values of j_e are excited with varying likelihoods. This is true even though the total XAS spectrum is invariant with respect to the direction of \hat{e} in the case of dipole transitions and cubic site symmetry. The various L_3 core holes have different energy distributions for the Auger electrons collected, and analysis of AES results allows one to “measure” the said likelihoods and—consequently—access the $d T_{2g}$, $d E_g$, and $s A_g$ partial densities of states (PDOSs). In a metal such as Ag, the unoccupied T_{2g} and E_g states are not as dramatically split as in a ligand cage. Nonetheless, these states have different PDOSs that can be separated *experimentally* as done in this work but would by virtue of cubic symmetry be impossible to separate from L_3 XAS alone.

Section II presents pertinent details of the experimental and theoretical methodology. This work involves XAS, AES, density-functional theory (DFT) calculations in the solid, atomic structure calculations, and consideration of the resonant-Auger analog of the Kramers–Heisenberg formula.¹ Section III presents XAS results, atomic AES results, results of line-shape modeling, solid-state AES results, and results for the unoccupied PDOS that rely on atomic theory alone. Section IV provides summary remarks and suggests potential directions for future work.

II. EXPERIMENTAL AND THEORETICAL METHODOLOGY

Experiments were performed at the National Institute of Standards and Technology beamline SST-2 at the National Synchrotron Light Source II, Brookhaven National Laboratory, on a commercially obtained Ag single crystal cut and polished to expose the {001} surface. X-ray absorption spectra were collected by monitoring sample drain current (total electron yield) versus incident photon energy in the vicinity of Ag spin-orbit split L_3 and L_2 XAS absorption edges (3351 and 3524 eV, respectively). Spectra were normalized to incident photon flux determined by photocurrent from a thin transmitting Al foil upstream of the sample. Auger electron spectra were recorded with a hemispherical electron analyzer operating in angular mode with a pass energy of either 50 or 200 eV, as required to maintain detector linearity.² The acceptance cone of the analyzer was aligned parallel to the x-ray electric-field polarization vector of the synchrotron beam. We used a liquid-nitrogen-cooled, double-crystal Si(220) monochromator that provided a 120 meV full width at half maximum (FWHM) photon energy spread at the Ag L_3 edge. Details of the beamline, vacuum system, and experimental procedures are given elsewhere.³⁻⁶

Two coordinate systems are relevant in this work. Unit vectors along the directions of the photon magnetic field, momentum, and electric field, respectively, \hat{b} , \hat{q} , and \hat{e} , define a coordinate system fixed by the beamline geometry, and these are useful as demonstrated in the Appendix. A second coordinate system (which rotates with the sample) has coordinates with unit vectors \hat{x} , \hat{y} , and \hat{z} . These are along the edges of silver's conventional (4 atom) face-centered cubic (fcc) unit cell. The sample was oriented with \hat{e} aligned along its [101] direction for the XAS measurements and along its [001] and [111] directions, respectively, denoted \hat{z} and $\hat{d} = (\sqrt{3}/3)(\hat{x} + \hat{y} + \hat{z})$, for the AES measurements. We use two coordinate systems because the core orbitals are most readily described in the (b, q, e) notation if their angular momenta are quantized along \hat{e} , whereas outer-shell and continuum states are most naturally described in a basis that is always oriented in a consistent fashion with respect to crystallographic directions.

The electronic structure was treated within DFT. The local-density approximation (LDA) was used in a plane-wave, pseudopotential framework. Additional details of the DFT calculations are given elsewhere.⁷ We used hard, $\{[\text{Ar}]3d^{10}\}$ -core norm-conserving pseudopotentials of the Hamann–Schlüter–Chiang type⁸ with Vanderbilt cutoff functions.⁹ We used a 100 Rydberg cutoff for the Bloch states. For the post-DFT calculations, we included the main corrections to the unoccupied LDA band structure based on the quasiparticle treatment by Marini *et al.*¹⁰ Bethe–Salpeter calculations were performed using OCEAN (Refs. 11–14) with 145 bands total (including the 4s and 4p bands) and Brillouin-zone grids with 1728 or 8000 k-points. This proved that results are converged with respect to k-point sampling at 1728 k-points and that photoelectron-core hole interactions did not affect the Auger results, other than changing the overall Auger yield in much the same way as the absorption spectrum.

Processes underlying AES results were modeled using the resonant-Augur version of the Kramers–Heisenberg formula that describes a system beginning in the ground state $|g\rangle$ and excited by a photon of energy $\epsilon = E_C + \omega$ (so that $\omega = 0$ eV at resonance, with E_C being the core-level binding energy relative to the Fermi level E_F). Excitation occurs by the dipole operator $\hat{e} \cdot \mathbf{r}$, with the electron position coordinate $\mathbf{r} = 0$ at the nucleus. The system is then in a superposition of intermediate excited states, in which ϵ_m is the photoelectron's quasiparticle energy relative to E_F in the presence of the L_3 hole,

$$|\Phi(\omega)\rangle = \sum_m \left(\frac{M_{mg}}{\omega - \epsilon_m + i\Gamma_C} \right) |m\rangle. \quad (1)$$

Here, $2\Gamma_C$ is the L_3 hole lifetime damping FWHM and $M_{mg} = \langle m | \hat{e} \cdot \mathbf{r} | g \rangle$. A state $|m\rangle$ can decay via the interaction between two $M_{4,5}$ ($3d$) electrons. One electron recombines with the L_3 hole and the other becomes the Auger electron that is detected. Each intermediate state $|m\rangle$ has a photoelectron and L_3 hole, and each final state $|f\rangle$ has the photoelectron, the Auger electron, and two $M_{4,5}$ holes with combined binding energy E_M . The distribution function for Auger electron energy E is

$$S(E) = C \sum_f \left| \sum_m \frac{M_{fm} M_{mg}}{(\omega - \epsilon_m + i\Gamma_C)} \right|^2 \delta(E_C + \omega - E_M - \epsilon_f - E). \quad (2)$$

This is nothing other than the Golden rule, with an overall prefactor C for completeness, and ϵ_f is the photoelectron's energy in the presence of the final-state core holes. A matrix element M_{fm} involves the Coulomb matrix element for two $M_{4,5}$ electrons interacting so that one fills the L_3 hole and the other is in an outgoing partial wave. The matrix element should also include a factor for the efficiency with which the Auger electron is detected. The delta function ensures that the photon energy equals the final-state energy shared by the core holes, photoelectron, and Auger electron,

$$E_C + \omega = E_M + \epsilon_f + E. \quad (3)$$

The prefactor C accounts for all relevant kinematical factors not mentioned, including a factor of 2 because of spin degeneracy of the unoccupied bands.

Energies ϵ_m and ϵ_f and the states associated with them should include the interaction of the photoelectron with the core hole(s). While XAS showed an enhancement of absorption because of interactions, especially close to the edge, the Auger results are presented in a way that is normalized to the absorption coefficient. As such, the Auger results are very weakly affected, so we ignored photoelectron-core hole interactions in the final state, which greatly simplifies calculations. By also ignoring the interactions in the intermediate state for purposes of simulating normalized AES data, each final state is related to one intermediate state with the photoelectron in the same Bloch state, but the final state also has the added degrees of freedom of Auger electron and two-hole core final-state quantum numbers. Because of lifetime damping, the final states associated with a nominal two-hole final state of the $M_{4,5}$ level form a Lorentzian distribution of states reflecting the core-hole lifetimes. Lifetime damping also arises because of the photoelectron, including the AES intermediate (XAS final) and AES final states. The calculated XAS and AES results included the damping of unoccupied states.

Atomic structure, core-level wave functions and energies, and final-state two-hole states were obtained using a relativistic, Hartree–Fock atomic program with a dense radial grid.¹⁵ Calculations were performed using both the Dirac equation, including determination of spin–orbit splitting, and the scalar-relativistic Koelling–Harmon equation¹⁶ plus spin–orbit interaction in a Pauli two-component framework. The calculations used limited configuration interaction, including all states with two $M_{4,5}$ holes and mixed coupling. The level scheme agrees with observed spectra and other calculations,¹⁷ including anomalous ordering of the 3F levels. Auger electron continuum states were treated in a spin–orbit-averaged scalar-relativistic framework. Because of the small (7° full-cone) solid angle for acceptance by the electron analyzer, which was centered around \hat{e} , it was only necessary to consider final states with Auger electron $l_e = 0$. In the calculations, it was also convenient to have all spin and orbital angular momenta quantized along that direction.

III. RESULTS AND ANALYSIS

A. XAS theory and experiment

The band structure and PDOS are shown in Fig. 1. The function describing the s PDOS passes smoothly through E_F but it has upticks at about 4.0 and 6.8 eV above E_F . This is because of the onset of the upper bands, at respective critical points L and X , split from the lower bands by zone-boundary level repulsion. There are concomitant upticks in the E_g and T_{2g} d PDOS, respectively, which dominate structure in XAS and Auger yields in Ag,¹⁸ Cu,¹⁹ and other face-centered cubic metals. Associating the E_g versus T_{2g} upticks with critical points as done above follows from tight-binding analysis.²⁰ Other effects involving core-hole degrees of freedom have been reported in coincidence experiments^{21,22} and x-ray fluorescence.²³ Measured and calculated absorption spectra and their derivatives with respect to photon energy are shown in Fig. 2. These include the core-hole lifetime (FWHM 2.0 eV²⁴) and electron lifetime damping in the conduction band.²⁵

B. Prediction and analysis of Auger spectra

The total XAS is the sum of contributions from core holes with every value of j_e in all subshells. One may decompose contributions from the L_3 subshell to the imaginary part of the dielectric constant according to

$$\epsilon_{2,L_3}(\epsilon) = \epsilon_{2,1/2}(\epsilon, \hat{e}) + \epsilon_{2,3/2}(\epsilon, \hat{e}). \quad (4)$$

The first term includes contributions from all states with $j_e = \pm 1/2$. The second does likewise for all states with $j_e = \pm 3/2$. By virtue of the cubic site symmetry and dominating dipole matrix elements, $\epsilon_2(\epsilon)$ is independent of \hat{e} , but the two terms appearing on the right-hand side depend on \hat{e} . The ratio of these two terms gives the ratio of the likelihood with which core holes are created for each value of $|j_e|$.

For Auger electrons emitted along \hat{e} , the Auger spectrum is a superposition of basis-function spectra, one for each value of $|j_e|$. Calculated Auger spectra for an isolated Ag⁺ ion emitting electrons along \hat{e} depends on j_e as shown in Fig. 3. In the solid, a simplified picture (which we adopt) would have such atomic spectra and their features convolved with a line shape that is discussed by Drube *et al.*¹⁸ and is a consequence of the resonant-Auger analog of the Kramers–Heisenberg equation.^{1,26} With the help of our Bethe–Salpeter equation (BSE) solver, we use the calculated $\epsilon_{2,j_e}(\epsilon)$ to perform a j_e -dependent convolution that considers the matrix-element-weighted density of unoccupied states that are dipole-allowed for each value of j_e .

Measured and calculated AES results are presented in Fig. 4 for two different incident photon energies: threshold or “resonance” (corresponding to transitions to the Fermi level and the first peak in the derivative XAS spectrum), and 15 eV above resonance where effects arising because of the crystalline band structure are less pronounced. The cartoon inset illustrates the overlap of a broadened region around the nominal photoelectron energy and the PDOS. The reverse shape of the overlap accounts for the Auger line shape at threshold, in accordance with the energy sharing in the final state as in Eq. (3). The mixture of Bloch

states in which the photoelectron finds itself in the intermediate states strongly affects the corresponding mixture in the final state. The latter mixture likewise affects the mixture of energies that the photoelectron has in the final state.

Measured spectra were normalized to the baseline above the Auger features and a Shirley background was subtracted to account for inelastic losses.²⁷ Calculated spectra were adjusted to make the value and slope of the curve equal to zero at the endpoints of the energy window shown. In the calculated spectra, there was still spectral weight on the low-kinetic-energy side reminiscent of an inelastic-loss background, but it was actually because of the low-energy tail of the Auger line shape and the photoelectron taking a larger share of the energy. The results in Fig. 4 exemplify many aspects of emitted Auger spectra. (Later, we will also discuss the dependence of results on $\hat{\epsilon}$.) Because of the line-shape asymmetry, spectral peaks are shifted down (in this case, by about 0.4 eV, with the shift depending on the core-hole widths). This is unlike in other systems that can exhibit an increased Auger energy at resonance, presumably because of interactions between the photoelectron (or other electrons) and the core hole.²⁸ Our present shift is consistent with having a “well-screened” or “noninteracting” system.

Furthermore, the effective resolution is enhanced near resonance, a hallmark of the resonant-Augur effect²⁹ fully realized here because of the narrow photon bandpass. Features labeled *a*, *d*, *e*, *f*, *g*, and *h* are, respectively, attributed to having 1S_0 , 1G_4 , 1D_2 , 3F_3 , 3F_2 , and 3F_4 two-hole final states on the core-excited site. Features label *b* and *c* (in the resonance case) are thought to be copies derived from the 1G_4 peak, with the photoelectron taking a greater fraction of the energy that it shares with the Auger electron in the final state. The feature labeled *b* is not as prominent in the measured resonance spectrum, but it is still evident. This PDOS and other effects of line shapes are discussed further in what follows.

Line shapes are shown in the top series of curves in Fig. 5 that assume an FWHM of 2.0 eV for an L_3 hole and an FWHM of 0.3 eV for a pair of $M_{4,5}$ holes in the 1G_4 state. The calculations use an analytical model for the line shape that assumes a step function for the unoccupied PDOS with the step up occurring at E_F . The model follows from Drube *et al.*¹⁸ and is derived in the Appendix. The figure shows the line-shape evolution over a range of photon energies from -3 to $+6$ eV relative to resonance. (Observed spectra are also integrated over a photon energy range because of the incident x-ray spectral width,¹⁸ but we neglect that small effect here.) Curves have been shifted so that $\epsilon' = 0$ corresponds to 2588.9 eV, the nominal location of the 1G_4 peak far above resonance. The Auger line shape resembles a left-right mirror image of the unoccupied PDOS, as discussed above, because the total energy must be conserved in the final state, with the total energy *shared* between the photoelectron and Auger electron. As a further consequence, the Fermi cut is observed at the high-energy flank of the Auger spectrum above resonance so that there is a step down in the line shape that begins around -3 eV and disperses to $+6$ eV in the successive curves. The step down weakens and eventually vanishes with increasing photon energy, effectively filling in the wings of a Lorentzian-like envelope function of the Auger peak well above threshold.

The maximum of the “line-shape function” disperses from below zero, because the peak of the Lorentzian is not yet filled in, but the energy position ceases to disperse around a

core-hole width above resonance. The step down that continues to disperse above resonance, however, is a signature of the Fermi edge being fixed in energy, and it is observable in spectra because it is an abrupt discontinuity in the PDOS that provides a fixed energy reference. The continuing dispersion of the Fermi step down above resonance is highly analogous to the “elastic” or “spectator” peak associated with a bound-state level in the PDOS that does continue to disperse well above threshold in other (typically nonmetallic) cases.³⁰ Such cases arise because of the localization of the photoelectron on the absorbing atom, a result of the bound state’s favorable cross section and the associated energy shift of the Auger peak at threshold relative to the main or “diagram” Auger line owing to this localization.²⁹

Because there is always a continuum of unoccupied states at higher energies than those to which the incident photon energy is tuned, the baseline appears raised on the low kinetic energy side, but this is really an aspect of the intrinsic Auger line shape. More generally, a spectrum found by convolving what is presented in Fig. 3 with the line shapes in Fig. 5 will also appear to have a raised baseline on the low-kinetic-energy side that is hard to distinguish from loss features and a secondary-electron background. The middle series of simulated Auger spectra for $\hat{e} = \hat{z}$ demonstrates this point. The illusion of a raised baseline on the high-energy side stems from two-hole final states at higher energies. In addition to the step down in the curves with the highest photon energies, the 1D_2 peak is also weakly seen as the photon energy approaches resonance from below. Measured spectra are shown in the bottom panel. There are noteworthy discrepancies between the simulated and measured spectra. The baseline is always higher in the measured case, especially at energies below the 1G_4 peak. The peak height is maximized at 4 eV in measured spectra, but at 5 eV in calculated spectra.

AES results are presented for photon energies -3 , $+0$, and $+1$ eV from resonance in Fig. 6, as calculated and measured. In both panels, spectra are normalized so that the curve varies between 0 and 1 for the energy region shown. Separation of the 3F_3 and 3F_2 peaks is clearly resolved at resonance. At about 4 and 6.6 eV below the main peak, there are copies of the 1G_4 peak. They are most visible well below resonance because of their relative enhancement. These copies follow from the reversed transcription of the PDOS that also underlies absorption spectra and is visible in Fig. 2 and are associated with the upticks in the PDOS. Although such structure in the PDOS persists well above the Fermi level, such features are washed out in the Auger spectrum at higher photon energies because of increasing electron damping. (Note that the spectrum recorded 15 eV above E_F in Fig. 4 shows little if any such structure.) Interestingly, some of the discrepancies in Fig. 6 are reminiscent of those in Fig. 2 when rotated by 180° . Incorporating additional inelastic losses to correct the calculated spectra can improve differences in the “baseline” on the low-energy side in the top panel, but deriving such losses is beyond the scope of this work. In Fig. 7, measured spectra are over a smaller energy region.

C. Determination of depopulation rates

For various combinations of photon energy ϵ and polarization vector \hat{e} , measured and calculated Auger spectra were considered over a kinetic-energy range from 2565 to 2610 eV.

Even after background subtraction, both spectra may have residual spectral weight on the low-kinetic-energy side of each peak. This may in part be a loss-induced artifact in measured spectra, but it is also a consequence of the Auger line shape. A cubic spline was, therefore, also subtracted from all spectra to set the value and derivative to zero at the endpoints to minimize baseline issues. (The experimental data were already corrected with a Shirley background.²⁷) We refer to the result following the spline subtraction as the “final spectrum” for a given (ϵ, \hat{e}) pair. Measured and calculated final spectra are shown in Fig. 8 with the 1G_4 peak normalized to equal peak height. Results for $\hat{e} = \hat{z}$ and $\hat{e} = \hat{d}$ are shown in red and blue, respectively, and the dependence of spectral features on \hat{e} is evident.

Using an even narrower energy range, between 2588 and 2609 eV, a final spectrum can be fitted to a linear combination of the atomic spectra shown in Fig. 3 convolved with the appropriate step-function-model line shape. This establishes the ratio of two quantities, $\epsilon_{2,1/2}(\epsilon, \hat{e})/\epsilon_{2,3/2}(\epsilon, \hat{e})$, whereas the sum of the two quantities is constrained by the total L_3 XAS. Numerical BSE results for $\epsilon_{2,j_e}(\epsilon)$ are shown in Fig. 9 for both polarizations, with minimal broadening. Smaller broadening was applied, which reveals artificial Brillouin-zone-sampling noise that is ordinarily washed out by lifetime-damping effects.

D. Determination of PDOS

We denote the dipole matrix element-weighted PDOS related to $d T_{2g}$, $d E_g$, and $s A_g$ partial waves by $\rho_T(\omega)$, $\rho_E(\omega)$, and $\rho_A(\omega)$, respectively. (As a reminder, the matrix elements are those for transitions from L_3 states.) One can also determine such quantities by analyzing measured XAS and AES data. As its input, the analysis only requires core-hole lifetime widths and the atomic, basis function spectra that should be easily found using standard tables and widely available atomic structure programs. We assume that the input PDOS (determining the line shape with which the basis functions are convolved) is a step function. In principle, the input and output PDOS could be made self-consistent by some iterative extension of our analysis, but here our analysis simply uses a step-function PDOS for its input, including when calculated Auger spectra are used in place of measured ones as a test.

We use the electric-dipole approximation and neglect the small effects of spin-orbit coupling on valence and unoccupied states. Thus, Bloch states are degenerate and the spin component along \hat{e} can always be considered a good quantum number, independent of the direction of \hat{e} . Hence, photoexcitation of an L_3 core electron can only make transitions to Bloch states because of $d T_{2g}$, $d E_g$, and $s A_g$ partial waves in the Bloch functions. As noted in the Appendix, cubic site symmetry ensures that interference effects because of cross-terms in squares of transition-matrix elements involving different partial-wave channels cannot contribute to the absorption spectrum. One may, therefore, deduce

$$\begin{aligned} D_{1/2}(\omega, \hat{e}) &= \frac{45\Omega_0}{8\pi^2} \epsilon_{2,1/2}(\epsilon, \hat{e}) = (12 - 9S_4)\rho_T(\omega) + (9S_4 - 1)\rho_E(\omega) + 10\rho_A(\omega), \\ D_{3/2}(\omega, \hat{e}) &= \frac{45\Omega_0}{8\pi^2} \epsilon_{2,3/2}(\epsilon, \hat{e}) = 9S_4\rho_T(\omega) + (9 - 9S_4)\rho_E(\omega) \end{aligned} \quad (5)$$

We define the normalization of $\rho_T(\omega)$, $\rho_E(\omega)$, $\rho_A(\omega)$ and S_4 in the Appendix. In the case of an amorphous sample, such as a sputtered Ag film, Eq. (5) becomes

$$\begin{aligned} D_{1/2}(\omega, \hat{e}) &= 11 \left(\frac{3\rho_T(\omega) + 2\rho_E(\omega)}{5} \right) + 10\rho_A(\omega), \\ D_{3/2}(\omega, \hat{e}) &= 9 \left(\frac{3\rho_T(\omega) + 2\rho_E(\omega)}{5} \right). \end{aligned} \quad (6)$$

Thus, the spherically averaged d and s PDOS can still be separately determined. This implies that the absorption spectrum (in this system) is a sum over partial absorption spectra that can be associated with the corresponding partial densities of states. This features the PDOS for only three of the ten irreducible representations of the O_h group, and we do not need to use double-group notation or theory because spin-orbit effects are not considered when describing the unoccupied states.

Analysis of Auger spectra for two different values of S_4 and XAS leads to three independent linear equations for $\rho_T(\omega)$, $\rho_E(\omega)$, and $\rho_A(\omega)$. The same analysis, however, does not give insight into any other PDOS, including that of $l=1$ partial-wave channels. The constraint formed by Eq. (4) ensures that Eq. (5) can lead to only three independent equations, even when multiple values of \hat{e} are considered. By virtue of cubic site symmetry, equations derived from Eq. (5) for any other value of S_4 would also be linearly dependent. Inverting these equations gives

$$\left. \begin{aligned} \rho_T(\omega) &= D_{3/2}(\omega, \hat{z}) / 9 \\ \rho_E(\omega) &= [3D_{3/2}(\omega, \hat{d}) - D_{3/2}(\omega, \hat{z})] / 18 \\ \rho_A(\omega) &= [D_{3/2}(\omega, \hat{z}) + 9D_{1/2}(\omega, \hat{z}) - 12D_{3/2}(\omega, \hat{d})] / 90 \end{aligned} \right\}. \quad (7)$$

Once the partial densities of states in Eq. (7) are known, one can *decompose* any XAS spectrum into associated components according to

$$\epsilon_{2, L_3}(\epsilon) = \frac{8\pi^2}{45\Omega_0} [12\rho_T(\omega) + 8\rho_E(\omega) + 10\rho_A(\omega)]. \quad (8)$$

One could also write $\epsilon_{2, L_3}(\epsilon) = \epsilon_{2, T}(\epsilon) + \epsilon_{2, E}(\epsilon) + \epsilon_{2, A}(\epsilon)$, with a partial absorption spectrum given by

$$\epsilon_{2, T}(\epsilon) = \frac{8\pi^2}{45\Omega_0} [12\rho_T(\omega)], \text{ etc.} \quad (9)$$

In Fig. 10, we show the results for the PDOS in terms of total and partial absorption spectra. A bold, black curve shows the theoretical XAS spectrum, and points shows the measured spectrum. The units of the vertical axis involve an arbitrary scale but are consistent for all quantities shown. Thin, dark curves show partial absorption spectra found using the BSE to calculate terms on the right-hand side of Eq. (5) for several values of \hat{e} and taking

appropriate sums and differences according to Eq. (7). The hollow points were obtained by analyzing the calculated Auger spectra. The filled circles with uncertainties shown were obtained by analyzing the measured Auger spectra. The uncertainty bars indicate the estimated standard uncertainty of a PDOS deduced from such measured spectra. The A_g PDOS inferred from the measured AES results is larger than what theory would suggest, perhaps because of inelastic losses not being taken fully into account, which can exaggerate the height of the 1G_4 peak. Hence, uncertainties regarding background subtraction propagate into uncertainties in the experimentally determined PDOS. In principle, it is also possible that the discrepancy highlights other approximations in the theory.

IV. SUMMARY

This work presents and analyzes Ag L_3 x-ray absorption and Ag $L_3 - M_{4,5}M_{4,5}$ Auger electron spectra. Auger electron spectra were analyzed in a manner dependent on photon polarization vector and electron emission direction. The results were used to determine the partial densities of states of unoccupied bands in Ag with no solid-state input. The extension of this work to other systems has great potential. One candidate system is Pd, where density-of-states effects of the empty $4d$ states just above the Fermi level could be observed, in contrast to the weaker density-of-states variations found in Ag. Another candidate class of system is tin oxides. There, a combination of ionicity and covalency affects the unoccupied densities of states.

The theory used in this work owes its success in part to the relative unimportance of electron-core hole and other interactions in noble metals. That is, a one-electron picture captures the important physics. In other systems, interactions could play a more significant role in not only affecting the relative importance of different resonant-Auger channels, but also giving rise to interference effects involving multiple channels. In this regard, interference effects can take place between different channels, even if the channels are not coupled by interactions in an intermediate state.

Ag, Pd, and tin oxides all have the advantage of having energetically accessible inner core levels (L_3) and deep outer core levels ($M_{4,5}$). This helps diminish the role of interactions between the Auger electron and final-state outer-core holes with the system. Interactions are Coulombic and involve banding effects on shallow core holes such as in Ge.³¹ Attention to interactions would also extend the value of this work to a wider class of materials, particularly where increased multipolar interactions between the photoelectron and core hole(s) are stronger.

Magnetic materials pose a different challenge to the assumptions made in this work. Magnetization and magnetic fields can affect time-reversal symmetry and the treatment of Bloch states' electron spin. It can also lead to linear and circular dichroism. It may also be worth considering whether magnetic dipole and electric quadrupole effects (which appear in the same order in the fine-structure constant) could be considered in XAS and concomitant AES spectra through a suitable adaptation of the present methodology. Such effects can give insight into occupancies of $4f$ shells in rare-earth systems.³² While we consider resonant

AES here, it also helps to consider connections between highly analogous spectroscopies, e.g., resonant and anomalous x-ray scattering,³³ and XAS.

ACKNOWLEDGMENTS

This research was performed at the National Institute of Standards and Technology (NIST) beamline SST-2 of the National Synchrotron Light Source II, a U.S. Department of Energy (DOE) Office of Science User Facility operated for the DOE Office of Science by Brookhaven National Laboratory under Contract No. DE-SC0012704.

DATA AVAILABILITY

The data that support the findings of this study are available from the corresponding author upon reasonable request.

APPENDIX

The L_3 XAS near-edge can be described by relating the imaginary part of the dielectric function to optically allowed transitions,

$$\epsilon_{2, L_3}(E_C + \omega) = \frac{4\pi^2}{\Omega_0} \sum_{ms, I} |\langle ms | \hat{e} \cdot \mathbf{r} | I \rangle|^2 \delta(\omega - \epsilon_m). \quad (\text{A1})$$

Here, we have $\epsilon = E_C + \omega$, where E_C is the photon energy at threshold (taking a core electron to the Fermi level). Note that nearly all the following analysis can be readily adapted to systems other than bulk materials and that the present analysis remains valid even in the presence of the central, attractive-potential part of the photoelectron-core hole interaction. The pair of indices, m and s , with $s = \pm$, sum over paramagnetic empty states. Thus, summing over m is like summing over unoccupied Bloch states, but the electron states should be evaluated in the presence of the core hole. The index I sums over L_3 core states. The position coordinate \mathbf{r} is relative to a nuclear coordinate, and ϵ_m is an electron level energy minus the Fermi level, E_F .

The wave function of a core state, using Pauli's two-component formalism, can be written as

$$\psi_I(\mathbf{r}) = R_C(r) \sum_{as} c_{Ias} Y_a(\hat{\mathbf{r}}) \chi_s. \quad (\text{A2})$$

(As mentioned in the main text, we used the scalar-relativistic, Koelling–Harmon equation with spin–orbit interaction included at the end within the space of the six Ag 2p levels. The strength of the spin–orbit splitting was found by solving the Dirac equation in the same atomic potential.) The radial dependence is given by $R_C(r)$. Letting b , q , and e denote components of \mathbf{r} along the magnetic field, momentum, and electric-field direction of an x-ray photon, the index a is b , q , or e , we have

$$Y_a(\hat{\mathbf{r}}) = \left(\frac{3}{4\pi}\right)^{1/2} \left(\frac{a}{r}\right), \quad (\text{A3})$$

and the spin index s can have values corresponding to a sign so that a two-component spinor is an eigenvector of the e spin component:

$$(\mathbf{e} \cdot \boldsymbol{\sigma})\chi_{\pm} = \pm \chi_{\pm}. \quad (\text{A4})$$

We let l be the e component (j_e) of the core state total angular momentum, j . If we introduce

$$Y_{\pm}(\hat{\mathbf{r}}) = \mp (1/2)^{1/2} [Y_b(\hat{\mathbf{r}}) \pm iY_q(\hat{\mathbf{r}})], \quad (\text{A5})$$

the c_{las} coefficients follow from

$$\psi_{\pm 3/2}(\mathbf{r}) = R_C(r)Y_{\pm}(\hat{\mathbf{r}})\chi_{\pm} \quad (\text{A6})$$

and

$$\psi_{\pm 1/2}(\mathbf{r}) = R_C(r)[(1/3)^{1/2}Y_{\pm}(\hat{\mathbf{r}})\chi_{\mp} + (2/3)^{1/2}Y_e(\hat{\mathbf{r}})\chi_{\pm}]. \quad (\text{A7})$$

In the core region, the wave function of an unoccupied state can be written as

$$\psi_{ms}(\mathbf{r}) = \sum_L b_{mL} R_L(\boldsymbol{\epsilon}_m, r) Y_L(\hat{\mathbf{r}}) \chi_s. \quad (\text{A8})$$

Each term in the sum has several factors. There is a radial dependence for each partial-wave channel, given by the real function $R_L(\boldsymbol{\epsilon}_m, r)$ multiplied by a mixing coefficient, b_{mL} . There is an angular factor $Y_L(\hat{\mathbf{r}})$, which is a real Kubik harmonic of angles measured with respect to crystallographic directions. There is also a spinor accounting for electron spin in the unoccupied state. This spin is quantized along $\hat{\mathbf{e}}$ for convenience. The direction of its quantization is irrelevant in the case of a paramagnetic system, to which the scope of this work is limited. The partial density of states for each channel is defined as

$$\rho_L(\omega) = \sum_m |f_L(\boldsymbol{\epsilon}_m) b_{mL}|^2 \delta(\omega - \boldsymbol{\epsilon}_m). \quad (\text{A9})$$

This is a matrix-element-weighted density of states, wherein matrix elements are evaluated within the electric-dipole approximation. The matrix element in that approximation involves the radial integral,

$$f_L(\boldsymbol{\epsilon}_m) = \int_0^{\infty} dr r^3 R_C(r) R_L(\boldsymbol{\epsilon}_m, r). \quad (\text{A10})$$

It is not necessary to choose the normalization of either $R_L(\boldsymbol{\epsilon}_m, r)$ or b_{mL} separately, but only that of their product. This is accomplished through knowledge of the absorption spectrum and its normalization. As usual, a PDOS is an arbitrary quantity regarding its normalization, radial weighting, etc., and it is important to know how it appears in equations in relation to other quantities, as is done here.

For each spin, six partial-wave channels are accessible by dipole transitions. They are the A_g s channel, for which the angular factor is

$$Y_{r^2} = \left(\frac{1}{4\pi}\right)^{1/2}, \quad (\text{A11})$$

the T_{2g} d channels, with

$$Y_{xy} = \left(\frac{15}{4\pi}\right)^{1/2} \frac{xy}{r^2}, \quad Y_{yz} = \left(\frac{15}{4\pi}\right)^{1/2} \frac{yz}{r^2}, \quad Y_{zx} = \left(\frac{15}{4\pi}\right)^{1/2} \frac{zx}{r^2}, \quad (\text{A12})$$

and the E_g d channels, with

$$\begin{aligned} Y_{x^2-y^2} &= \frac{1}{2} \left(\frac{15}{4\pi}\right)^{1/2} \left(\frac{x^2-y^2}{r^2}\right), \\ Y_{3z^2-r^2} &= \frac{1}{2} \left(\frac{5}{4\pi}\right)^{1/2} \left(\frac{2z^2-x^2-y^2}{r^2}\right). \end{aligned} \quad (\text{A13})$$

Therefore, the label L can be r^2 , xy , yz , zx , $x^2 - y^2$, or $3z^2 - r^2$. The Y functions are normalized on the unit sphere. Site symmetry implies there are three independent partial densities of states,

$$\rho_T(\epsilon_m) = \rho_{xy}(\epsilon_m) = \rho_{yz}(\epsilon_m) = \rho_{zx}(\epsilon_m), \quad (\text{A14})$$

$$\rho_E(\epsilon_m) = \rho_{x^2-y^2}(\epsilon_m) = \rho_{3z^2-r^2}(\epsilon_m), \quad (\text{A15})$$

and

$$\rho_A(\epsilon_m) = \rho_{r^2}(\epsilon_m), \quad (\text{A16})$$

whereas a matrix element in Eq. (A1) is

$$\begin{aligned} \langle ms | \hat{\mathbf{e}} \cdot \mathbf{r} | I \rangle &= \left(\frac{4\pi}{3}\right)^{1/2} \sum_{L, as'} (b_{mL})^* c_{Ias'} \delta_{ss'} f_L(\epsilon_m) \\ &\times \int d^2\hat{\mathbf{r}} Y_L^*(\hat{\mathbf{r}}) Y_e(\hat{\mathbf{r}}) Y_a(\hat{\mathbf{r}}). \end{aligned} \quad (\text{A17})$$

Using the same decomposition as Eq. (4), we have

$$\begin{aligned} \epsilon_{2,J}(\epsilon) &= \frac{4\pi^2}{\Omega_0} \sum_{ms} \sum_{I = \pm J} \delta(\omega - \epsilon_m) \\ &\times \int d^3\mathbf{r} \int d^3\mathbf{r}' \psi_{ms}^\dagger(\mathbf{r}) (\hat{\mathbf{e}} \cdot \mathbf{r}) \psi_I(\mathbf{r}) \psi_I^\dagger(\mathbf{r}') (\hat{\mathbf{e}} \cdot \mathbf{r}') \psi_{ms}(\mathbf{r}'), \end{aligned} \quad (\text{A18})$$

with $J = 1/2$ or $J = 3/2$. The function $\psi_{ms}(\mathbf{r}')$ is the product of a scalar that is independent of s and the spinor χ_s , and likewise for $\psi_{ms}^\dagger(\mathbf{r})$, so χ_s and its adjoint are the only ways that

the integrand depends on s . One can carry out the following sums over s and I within the integrand and use the spherical harmonics addition theorem to obtain the following equation:

$$\begin{aligned} & \sum_s \sum_{I = \pm 3/2} \chi_s^\dagger \psi_I(\mathbf{r}) \psi_I^\dagger(\mathbf{r}') \chi_s \\ &= R_C(r) R_C(r') [Y_{\pm}^*(\hat{\mathbf{r}}) Y_{\pm}(\hat{\mathbf{r}}') + Y_{\mp}^*(\hat{\mathbf{r}}) Y_{\mp}(\hat{\mathbf{r}}')] \\ &= \frac{3}{4\pi} R_C(r) R_C(r') [\hat{\mathbf{r}} \cdot \hat{\mathbf{r}}' - (\hat{\mathbf{e}} \cdot \hat{\mathbf{r}})(\hat{\mathbf{e}} \cdot \hat{\mathbf{r}}')] \end{aligned} \quad (\text{A19})$$

and

$$\begin{aligned} & \sum_s \sum_{I = \pm 1} \chi_s^\dagger \psi_I(\mathbf{r}) \psi_I^\dagger(\mathbf{r}') \chi_s \\ &= R_C(r) R_C(r') \left\{ \frac{1}{3} [Y_{\pm}^*(\hat{\mathbf{r}}) Y_{\pm}(\hat{\mathbf{r}}') + Y_{\mp}^*(\hat{\mathbf{r}}) Y_{\mp}(\hat{\mathbf{r}}')] + \frac{4}{3} Y_e^*(\hat{\mathbf{r}}) Y_e(\hat{\mathbf{r}}') \right\} \\ &= \frac{1}{4\pi} R_C(r) R_C(r') [\hat{\mathbf{r}} \cdot \hat{\mathbf{r}}' + 3(\hat{\mathbf{e}} \cdot \hat{\mathbf{r}})(\hat{\mathbf{e}} \cdot \hat{\mathbf{r}}')]. \end{aligned} \quad (\text{A20})$$

In Eq. (A18), a replacement $m \rightarrow M$ $m \in M$ would regroup final states into each set M of degenerate states related by symmetry. Consider the sum of probability densities of a given set,

$$\sum_{m \in M} \left[\sum_L \sum_L b_{mL}^* R_L(\boldsymbol{\epsilon}_m, r) Y_L^*(\hat{\mathbf{r}}) \right] \left[\sum_{L'} b_{mL'} R_{L'}(\boldsymbol{\epsilon}_m, r) Y_{L'}(\hat{\mathbf{r}}) \right]. \quad (\text{A21})$$

Because of cubic site symmetry, this must also have cubic symmetry. This can only be true if sums over terms with $L \neq L'$ are zero. One, therefore, has

$$\begin{aligned} & \sum_{m \in M} \left[\sum_L b_{mL}^* R_L(\boldsymbol{\epsilon}_m, r) Y_L^*(\hat{\mathbf{r}}) \right] \left[\sum_{L'} b_{mL'} R_{L'}(\boldsymbol{\epsilon}_m, r) Y_{L'}(\hat{\mathbf{r}}) \right] \\ &= \sum_{m \in M} \sum_L R_L(\boldsymbol{\epsilon}_m, r) R_L(\boldsymbol{\epsilon}_m, r') |b_{mL}|^2 Y_L^*(\hat{\mathbf{r}}) Y_L(\hat{\mathbf{r}}'). \end{aligned} \quad (\text{A22})$$

Thus, double summation over L and L' collapses to single summation over L , which can be taken outside the integrals, making integrations over radial and angular coordinates separable. Furthermore, although s and multiple d states may be simultaneously featured in any given Bloch state, the absorption spectrum is a sum over partial spectra without any net interference effects because of partial waves belonging to different values of L . Using the results of Eqs. (A19)-(A22) and Eqs. (A9) and (A10), Eq. (A18) becomes

$$\left. \begin{aligned} \epsilon_{2,3/2}(\boldsymbol{\epsilon}) &= \frac{3\pi}{\Omega_0} \sum_L \rho_L(\omega) (A_L - B_L) \\ \epsilon_{2,1/2}(\boldsymbol{\epsilon}) &= \frac{\pi}{\Omega_0} \sum_L \rho_L(\omega) (A_L + 3B_L) \end{aligned} \right\}, \quad (\text{A23})$$

with

$$A_L = \int d^2\hat{r} \int d^2\hat{r}' Y_L^*(\hat{r}) Y_L(\hat{r}') (\hat{r} \cdot \hat{r}') (\hat{e} \cdot \hat{r}) (\hat{e} \cdot \hat{r}') \quad (\text{A24})$$

and

$$B_L = \int d^2\hat{r} \int d^2\hat{r}' Y_L^*(\hat{r}) Y_L(\hat{r}') (\hat{e} \cdot \hat{r})^2 (\hat{e} \cdot \hat{r}')^2. \quad (\text{A25})$$

From completeness, we have $\int d^2\hat{r} Y_L^*(\hat{r}) Y_L(\hat{r}) = 4\pi/3$ and $\int d^2\hat{r} Y_L^*(\hat{r}) Y_L(\hat{r}) (\hat{e} \cdot \hat{r})^2 = 4\pi/5$. Letting e_x denote $\hat{e} \cdot \hat{x}$, etc., we note $e_x^2 + e_y^2 + e_z^2 = (e_x^2 + e_y^2 + e_z^2)^2 = S_4 + 2(e_x^2 e_y^2 + e_y^2 e_z^2 + e_z^2 e_x^2) = 1$, with $S_4 = e_x^4 + e_y^4 + e_z^4$. Because a Y_L is either even or odd with respect to each Cartesian coordinate of \hat{r} or \hat{r}' , one has

$$A_L = \int d^2\hat{r} \int d^2\hat{r}' Y_L^*(\hat{r}) Y_L(\hat{r}') [e_x^2(x^2 x'^2 + xyx'y' + xzx'z') + \dots]. \quad (\text{A26})$$

Inspecting Eq. (A26) and using completeness gives $A_{r^2} = 4\pi/9$, $A_{xy} + A_{yz} + A_{zx} = 8\pi/15$ and $A_{x^2-y^2} + A_{3z^2-r^2} = 16\pi/45$. Using

$$\begin{aligned} (\hat{e} \cdot \hat{r})^2 &= \frac{1}{3} P_0(\hat{e} \cdot \hat{r}) + \frac{2}{3} P_2(\hat{e} \cdot \hat{r}) \\ &= \frac{4\pi}{3} Y_{r^2}^*(\hat{e}) Y_{r^2}(\hat{r}) + \frac{8\pi}{15} \sum_{L=xy,yz,zx,x^2-y^2,3z^2-r^2} Y_L^*(\hat{e}) Y_L(\hat{r}), \end{aligned} \quad (\text{A27})$$

and the analogous equation for \hat{r}' , one obtains $B_{r^2} = 4\pi/9$, $B_{xy} + B_{yz} + B_{zx} = (8\pi/15)(1 - S_4)$, and $B_{x^2-y^2} + B_{3z^2-r^2} = (8\pi/45)(3S_4 - 1)$. Equation (5) follows from this and Eq. (A23).

Instead of considering transitions enumerated by pairs of values (m_s, l), suppose that spectra for each pair of values (I, L) can be computed independently. This is true in the present case, even when the main, central part of the electron-core hole interaction is included. What follows applies within the framework of a single (I, L) channel of the resonant-Auger process. For monochromatic light, an Auger line shape can be re-expressed in terms of the function

$$\begin{aligned} f(E') &= B \int_0^\infty dE \mu(E) \left(\frac{1}{(E - \omega)^2 + \Gamma_L^2} \right) \\ &\quad \times \left(\frac{1}{(E - \omega + E')^2 + \Gamma_M^2} \right). \end{aligned} \quad (\text{B1})$$

In the present notation, Γ_L and Γ_M are the *half*-widths of L_3 (one hole) and $M_{4,5}M_{4,5}$ (two-hole) states. Energy scales are shifted so that $E = 0$ occurs for a state with an L_3 hole and the photoelectron at the Fermi level, ω is the difference between photon energy and the L_3 threshold energy, and E' is the amount by which the Auger electron's energy deviates from the difference between L_3 and $M_{4,5}M_{4,5}$ binding energies. The density of intermediate

states of the overall wave function, $\mu(E)$, includes matrix elements, whereas B addresses all other prefactors pertinent to Auger decay.

In the simple case of $\mu(E) = \mu_0\theta(E)$, one may introduce $z = E - \omega$ and apply the method of partial fractions twice to find

$$\begin{aligned}
 f(E') &= B\mu_0 \int_{-\omega}^{\infty} dz \left(\frac{1}{z^2 + \Gamma_L^2} \right) \left(\frac{1}{(z + E')^2 + \Gamma_M^2} \right) \\
 &= \frac{B\mu_0}{4\Gamma_L\Gamma_M} \int_{-\omega}^{\infty} dz \left(\frac{1}{z - i\Gamma_L} - \frac{1}{z + i\Gamma_L} \right) \left(\frac{1}{z + E' + i\Gamma_M} - \frac{1}{z + E' - i\Gamma_M} \right) \\
 &= \frac{B\mu_0}{4\Gamma_L\Gamma_M} \int_{-\omega}^{\infty} dz \left[+ \frac{1}{E' + i\Gamma_L + i\Gamma_M} \left(\frac{1}{z - i\Gamma_L} - \frac{1}{z + E' + i\Gamma_M} \right) \right. \\
 &\quad - \frac{1}{E' + i\Gamma_L - i\Gamma_M} \left(\frac{1}{z - i\Gamma_L} - \frac{1}{z + E' - i\Gamma_M} \right) \\
 &\quad - \frac{1}{E' - i\Gamma_L + i\Gamma_M} \left(\frac{1}{z + i\Gamma_L} - \frac{1}{z + E' + i\Gamma_M} \right) \\
 &\quad \left. + \frac{1}{E' - i\Gamma_L - i\Gamma_M} \left(\frac{1}{z + i\Gamma_L} - \frac{1}{z + E' - i\Gamma_M} \right) \right]. \tag{B2}
 \end{aligned}$$

The first and fourth terms in square brackets are complex conjugates. Regarding the first term, one has

$$\frac{1}{E' + i\Gamma_L + i\Gamma_M} = \frac{E' - i(\Gamma_L + \Gamma_M)}{E'^2 + (\Gamma_L + \Gamma_M)^2} \tag{B3}$$

and

$$\begin{aligned}
 &\int_{-\omega}^{\infty} dz \left(\frac{1}{z - i\Gamma_L} - \frac{1}{z + E' + i\Gamma_M} \right) \\
 &= \Lambda(\omega, E') + i\pi + i \tan^{-1} \left(\frac{\omega}{\Gamma_L} \right) + i \tan^{-1} \left(\frac{\omega - E'}{\Gamma_M} \right), \tag{B4}
 \end{aligned}$$

with

$$\Lambda(\omega, E') = \frac{1}{2} \log_e \left(\frac{(\omega - E')^2 + \Gamma_M^2}{\omega^2 + \Gamma_L^2} \right). \tag{B5}$$

[For each term in the integrand Eq. (B4), one may integrate along a circular arc on which the magnitude of the denominator is constant, clockwise if below the real axis, counterclockwise if above, to where the denominator is real and positive, and from there along a horizontal contour in the $+z$ direction. Because contributions from beyond where the denominators exceed the larger denominator's magnitude cancel, the integration of both terms can stop there. Remaining integrations at an arbitrarily large, positive real part of z to return z to the real axis vanish.] The second and third terms are also complex conjugates. Regarding the second term, one has

$$\frac{1}{E' + i\Gamma_L - i\Gamma_M} = \frac{E' - i(\Gamma_L - \Gamma_M)}{E'^2 + (\Gamma_L - \Gamma_M)^2} \quad (\text{B6})$$

and

$$\begin{aligned} \int_{-\omega}^{\infty} dz \left(\frac{1}{z - i\Gamma_L} - \frac{1}{z + E' - i\Gamma_M} \right) \\ = \Lambda(\omega, E') + i \tan^{-1} \left(\frac{\omega}{\Gamma_L} \right) - i \tan^{-1} \left(\frac{\omega - E'}{\Gamma_M} \right). \end{aligned} \quad (\text{B7})$$

Substituting (B3)-(B7) into (B2) gives

$$\begin{aligned} f(E') = \frac{B\mu_0 E'}{2\Gamma_L \Gamma_M} \left(\frac{1}{E'^2 + (\Gamma_L + \Gamma_M)^2} - \frac{1}{E'^2 + (\Gamma_L - \Gamma_M)^2} \right) \Lambda(\omega, E') \\ + \frac{B\mu_0}{2\Gamma_L \Gamma_M} \left(\frac{\Gamma_L + \Gamma_M}{E'^2 + (\Gamma_L + \Gamma_M)^2} \right) \left[\tan^{-1} \left(\frac{\omega}{\Gamma_L} \right) + \tan^{-1} \left(\frac{\omega - E'}{\Gamma_M} \right) + \pi \right] \\ - \frac{B\mu_0}{2\Gamma_L \Gamma_M} \left(\frac{\Gamma_L - \Gamma_M}{E'^2 + (\Gamma_L - \Gamma_M)^2} \right) \left[\tan^{-1} \left(\frac{\omega}{\Gamma_L} \right) - \tan^{-1} \left(\frac{\omega - E'}{\Gamma_M} \right) \right]. \end{aligned} \quad (\text{B8})$$

Although the denominators with $\Gamma_L - \Gamma_M$ can become small when both $\Gamma_L - \Gamma_M$ and E' approach zero, the terms in Eq. (B8) are all still well-behaved.

If ω is large and positive, the quantity in brackets on the second line in Eq. (B8) approaches 2π for small E' so that $f(E')$ approaches a Lorentzian with an FWHM of $2(\Gamma_L + \Gamma_M)$. If ω is large but negative, the last factor in the integrand in Eq. (B1) is a Lorentzian peaked at $E = -E' - |\omega|$. This Lorentzian is more fully sampled if we have $E' < |\omega|$, in which case a factor of $1 / (E'^2 + \Gamma_L^2)$ can be taken outside the integral with minor approximation.

Evolution of $f(E')$ at intermediate ω is not trivial. At $\omega = 0$, the second and third lines of Eq. (B8) give rise to Lorentzian times combinations of constants and smoothed step functions. These serve to transform a Lorentzian-like function into one that is enhanced for $E' < 0$ and suppressed for $E' > 0$, with its peak shifted to negative E' . The first line of Eq. (B8) crosses zero at $E' = 0$ but falls off for large E' of either sign. The sign of its zero crossing is positive for $\Gamma_L > \Gamma_M$ and negative otherwise. In the former case, which occurs frequently, it slightly weakens the distortions associated with the second and third lines alone. At $\omega = 0$, the overall broadening and off-centering increase with Γ_L , but anticipating widths is most easily accomplished by evaluating Eq. (B8) or even Eq. (B1) and observing the outcome.

REFERENCES

1. Åberg T and Crasemann B, in Resonant Anomalous X-Ray Scattering Theory and Applications, edited by Materlik G, Sparks CJ, and Fischer K (North-Holland, Amsterdam, 1994), p. 431.

2. Weiland C, Browning R, Karlin BA, Fischer DA, and Woicik JC, *Rev. Sci. Instrum* 84, 036106 (2013). [PubMed: 23556858]
3. Weiland C, Rumaiz AK, Lysaght P, Karlin B, Woicik JC, and Fischer D, *J. Electron Spectrosc. Relat. Phenom* 190, 193 (2013).
4. Weiland C et al., *Synchrotron Radiat. News* 31, 23 (2018).
5. Woicik JC, Weiland C, and Rumaiz AK, *Phys. Rev. B* 91, 201412(R) (2015).
6. Woicik JC, Weiland C, Rumaiz AK, Brumbach M, Quackenbush NF, Ablett JM, and Shirley EL, *Phys. Rev. B* 98, 115149 (2018).
7. Shirley EL, Terminello LJ, Klepeis JE, and Himpsel FJ, *Phys. Rev. B* 53, 10296 (1996).
8. Hamann DR, Schlüter M, and Chiang C, *Phys. Rev. Lett* 43, 1494 (1979).
9. Vanderbilt D, *Phys. Rev. B* 32, 8412 (1985).
10. Marini A, Del Sole R, and Onida G, *Phys. Rev. B* 66, 115101 (2002).
11. Vinson J, Rehr JJ, Kas JJ, and Shirley EL, *Phys. Rev. B* 83, 115106 (2011).
12. Gilmore K, Vinson J, Shirley EL, Prendergast D, Pemmaraju CD, Kas JJ, Vila FD, and Rehr JJ, *Comput. Phys. Commun* 197, 109 (2015).
13. Vinson J and Shirley EL, *Phys. Rev. B* 103, 245143 (2021).
14. Shirley EL, Vinson J, and Gilmore K, "The OCEAN suite: Core excitations," in *International Tables for Crystallography* (Wiley, New York, NY, 2020), Vol. I.
15. Shirley EL, "Quasiparticle calculations in atoms and many-body core-valence partitioning," Ph.D. thesis (University of Illinois at Urbana-Champaign, 1991).
16. Koelling DD and Harmon BN, *J. Phys. C: Solid State Phys* 10, 3107 (1977).
17. Kleiman GG, de Castro SGC, and Landers R, *Phys. Rev. B* 49, 2753 (1994).
18. Drube W, Treusch R, and Materlik G, *Phys. Rev. Lett* 74, 42 (1995). [PubMed: 10057694]
19. Föhlisch A, Karis O, Weinelt M, Hasselström J, Nilsson A, and Mårtensson N, *Phys. Rev. Lett* 88, 027601 (2001). [PubMed: 11801036]
20. Harrison WA, *Electronic Structure and the Properties of Solids* (Dover, New York, 1980).
21. Gotter R, Da Pieve F, Ruocco A, Offi F, Stefani G, and Bartynski RA, *Phys. Rev. B* 72, 235409 (2005).
22. Gotter R, Da Pieve F, Offi F, Ruocco A, Verdini A, Yao H, Bartynski R, and Stefani G, *Phys. Rev. B* 79, 075108 (2009).
23. Southworth SH, Lindle DW, Mayer R, and Cowan PL, *Phys. Rev. Lett* 67, 1098 (1991). [PubMed: 10045075]
24. Campbell JL and Papp T, *At. Data Nucl. Data Tables* 77, 1 (2001).
25. Shirley EL, *Radiat. Phys. Chem* 167, 108165 (2020).
26. Åberg T, *Phys. Scr T41*, 71 (1992).
27. Shirley DA, *Phys. Rev. B* 5, 4709 (1972).
28. Woicik JC, Weiland C, and Rumaiz AK, *Phys. Rev. B* 91, 201412 (2015).
29. Armen GB, Aksela H, Åberg T, and Aksela S, *J. Phys. B: At., Mol. Opt. Phys* 33, R49 (2000).
30. Guillemin R et al., *Phys. Rev. A* 92, 012503 (2015).
31. Antonides E, Jansen EC, and Sawatzky GA, *Phys. Rev. B* 15, 1669 (1977).
32. Brown SD, Strange P, Bouchenoire L, and Thompson PBJ, *Phys. Rev. B* 87, 165111 (2013).
33. Arola E, Strange P, and Gyorffy BL, *Phys. Rev. B* 55, 472 (1997).

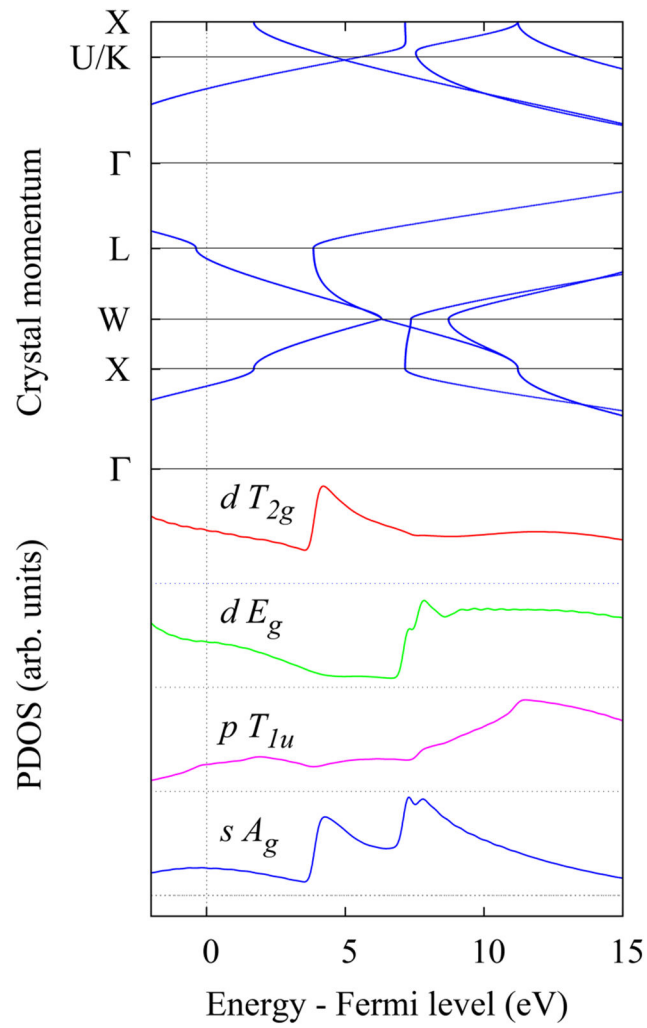


FIG. 1. Ag band structure and PDOS decomposed by symmetry. The PDOS in this figure was evaluated on a dense Brillouin-zone grid and minimally broadened.

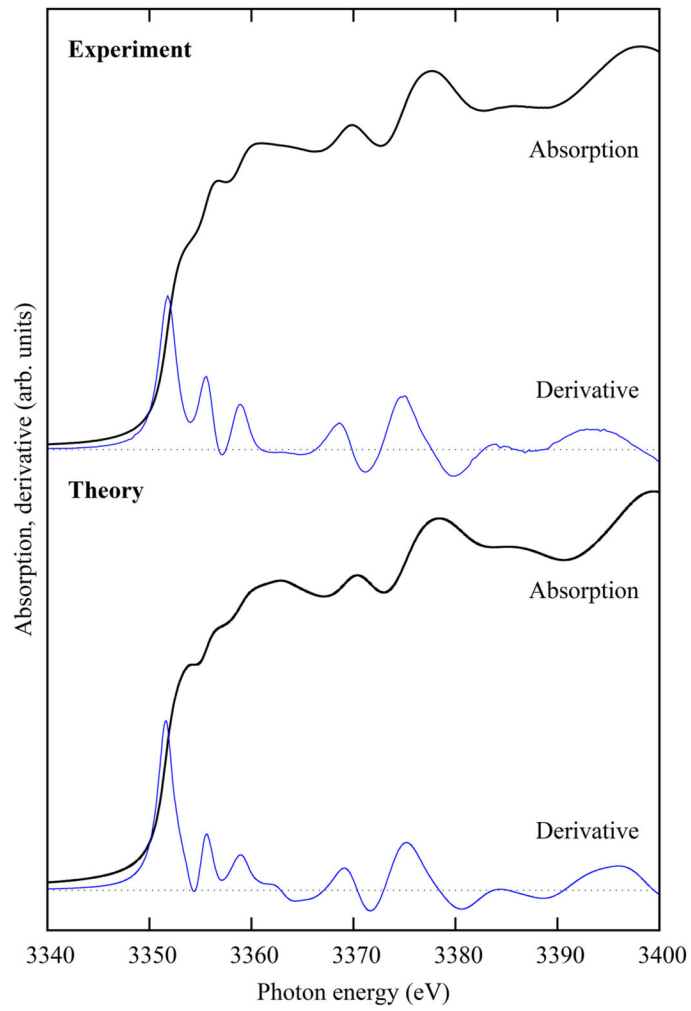


FIG. 2. Ag L_3 edge absorption spectrum (black, heavy line) and its derivative (blue, thin line) as measured and calculated.

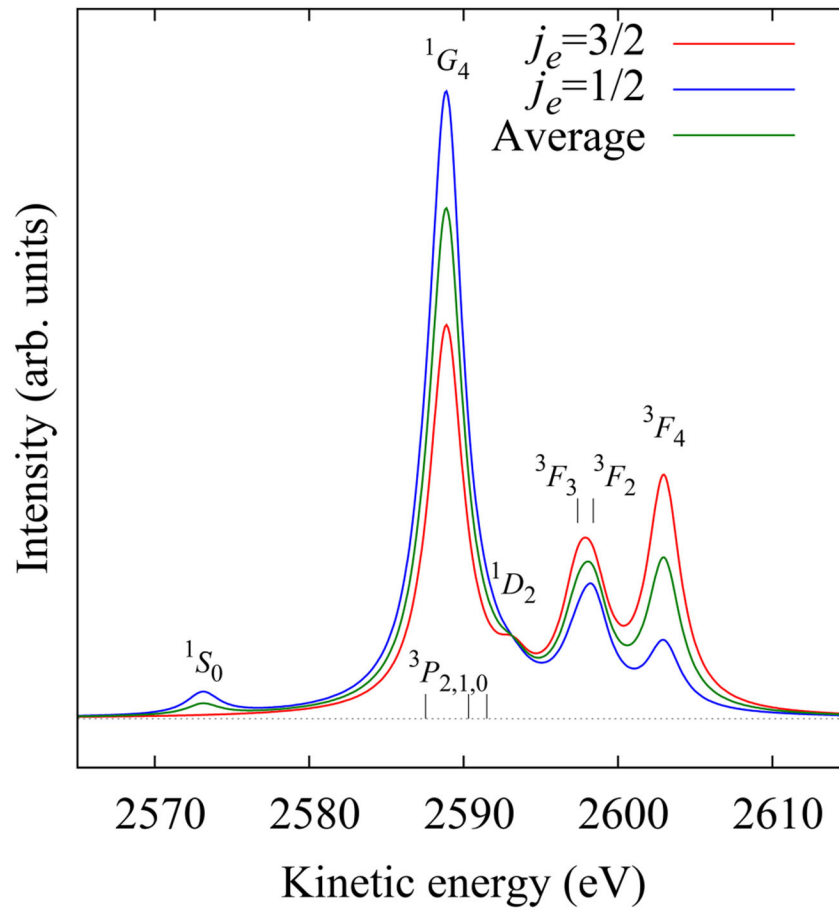


FIG. 3.

Ag $L_3 - M_{4,5}M_{4,5}$ Auger spectrum for electrons emitted along the \hat{e} direction, along which the $2p_{3/2}$ hole total angular momentum has been quantized. Results are shown for two of the hole states, along with an average spectrum that is proportional to what would be observed if emission were integrated over all directions for any $2p_{3/2}$ hole. All peaks are assigned. Those that are discernible here or in some measured spectra are indicated with a term symbol above the peak. The $3P_{2,1,0}$ levels are not discerned, and their positions are only indicated on the horizontal axis.

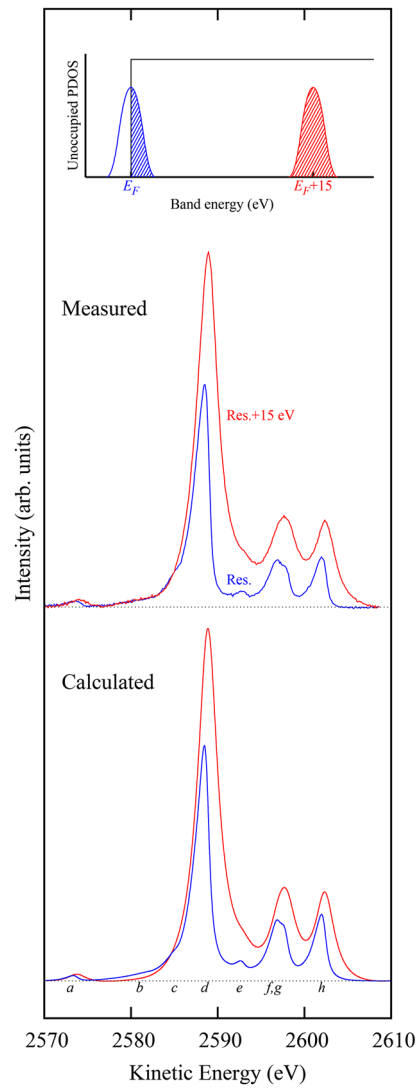


FIG. 4. Measured (top) and calculated (bottom) Ag $L_3 - M_{4,5}M_{4,5}$ Auger spectra for two incident photon energies. The letters used to indicate spectral features are discussed in the text. The schematic shows a step-function model for the unoccupied PDOS. At resonance, the region shaded blue indicates photoelectron states emphasized in the resonant-Auger process and their relative significance. The region shaded red indicates the same for excitation far above resonance.

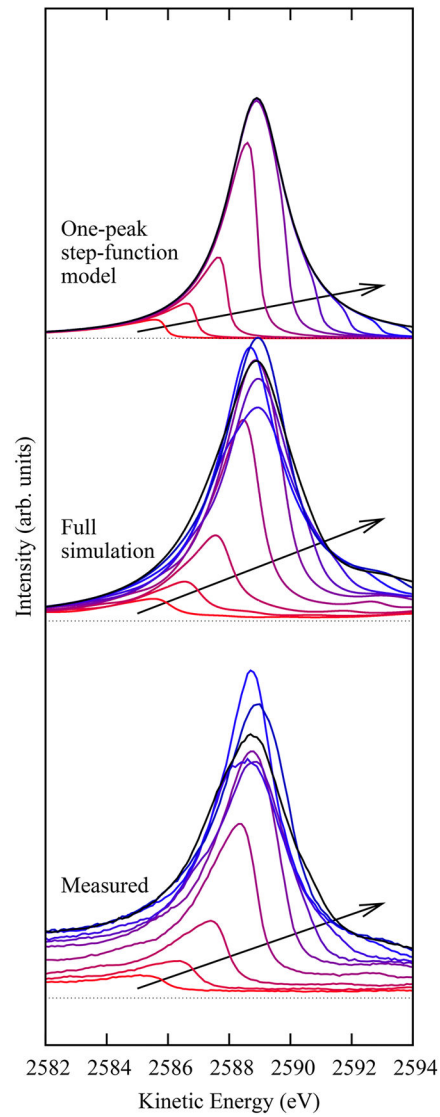


FIG. 5. Simulation and experiment for Auger line-shape evolution for a single two-hole final-state level (or full spectrum) as described in the text. Top: Step-function PDOS, single-level simulation, middle: calculated Auger spectrum, and bottom: measured Auger spectrum. Spectra are shown for photon energies varying from -3 to $+6$ eV relative to resonance in 1 eV steps with increasing steps indicated by the arrows. The color legend goes from red to purple to blue to black.

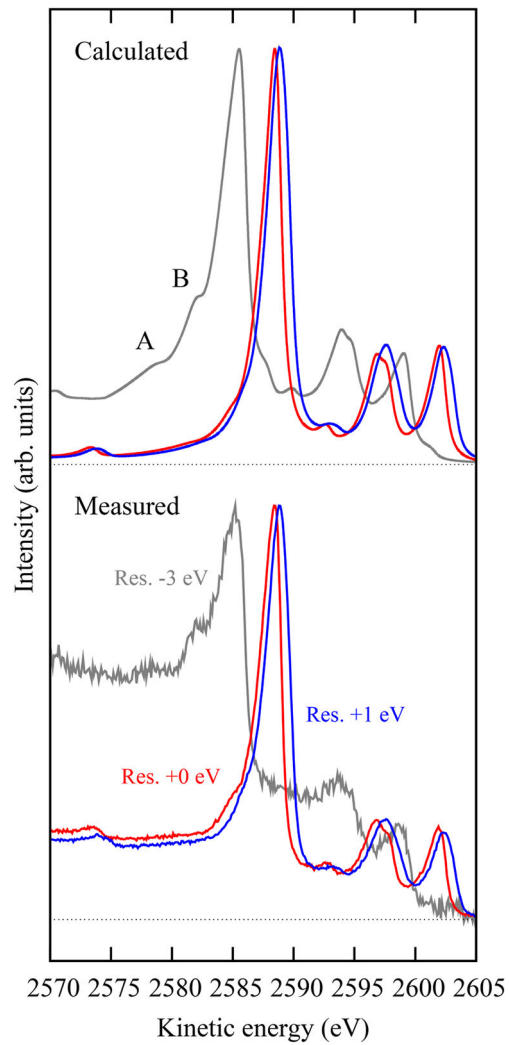


FIG. 6. Calculated and measured Ag $L_3 - M_{4,5}M_{4,5}$ Auger spectra for photon energy tuned to -3 , $+0$, and $+1$ eV from resonance. In the -3 eV case, the spectrum has copies of the 1G_4 peak shifted down by about 4 eV (B) and 6.6 eV (A). These can be traced to PDOS upticks shown in Fig. 1.

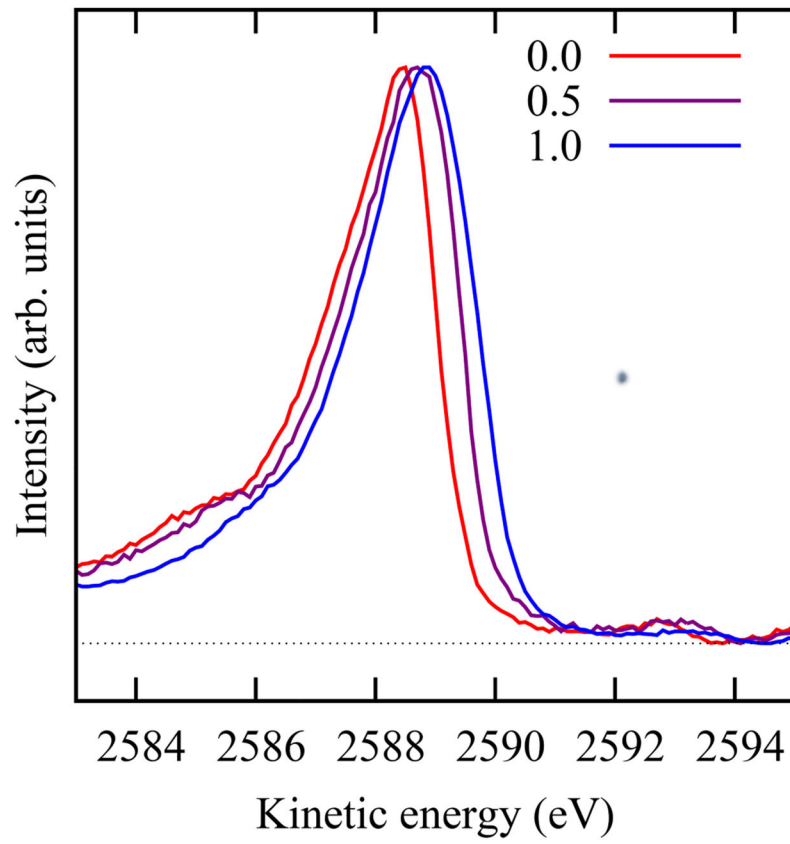


FIG. 7. Measured AES spectra, magnifying the region around the 1G_4 peak. The incident photon energy relative to resonance is indicated.

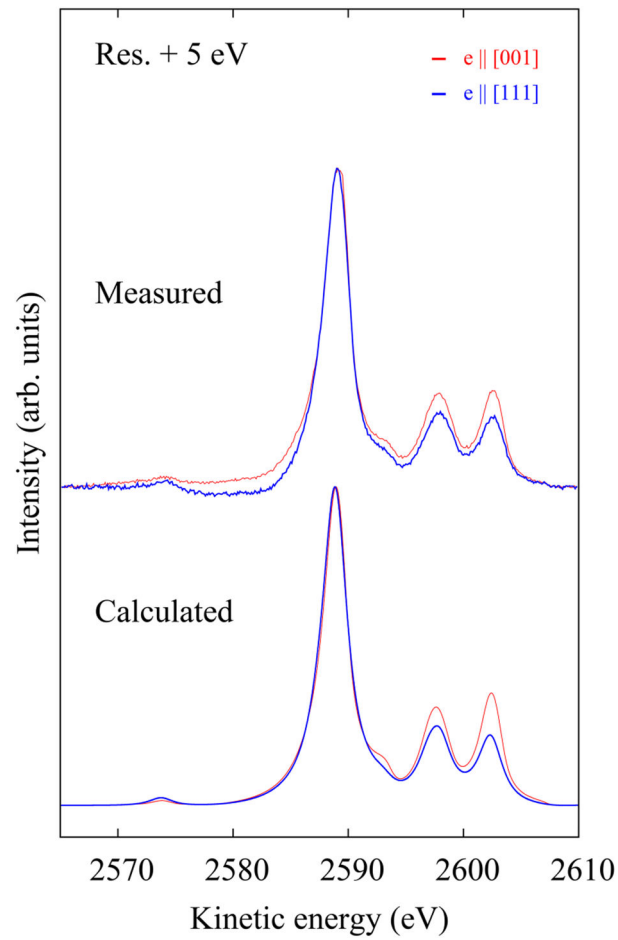


FIG. 8. Measured and calculated Ag $L_3 - M_{4,5}M_{4,5}$ Auger spectra for two polarizations at 5 eV above resonance. The curves for $\hat{e} \parallel \hat{z}$ are red and higher, and the curves for $\hat{e} \parallel \hat{d}$ are blue and lower. The polarization dependence of measured results around 2580 eV, which is not predicted, is conjectured to arise in part from unaccounted losses referenced to the ${}^3F_{3,2,4}$ peaks that are relatively enhanced for $\hat{e} \parallel \hat{z}$. All spectra are normalized to have the same maximum peak height.

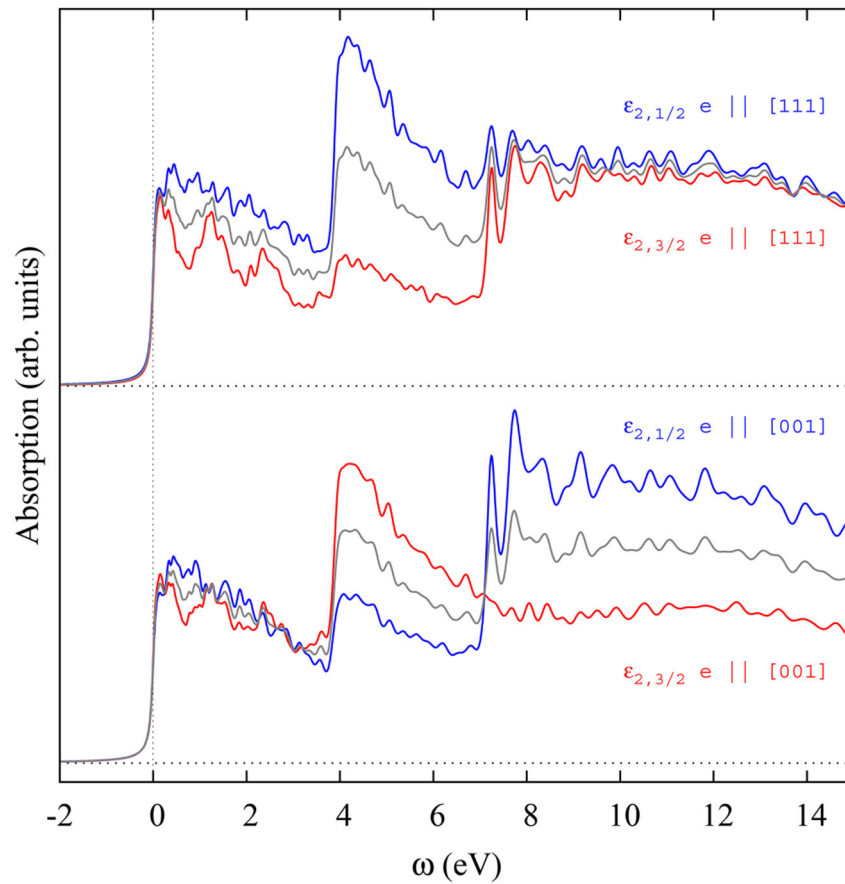


FIG. 9. Calculated partial absorption spectra of the form $\epsilon_{2,j_e}(\epsilon, \hat{e})$ for polarization along the [111] and [001] directions. Here, ω is the difference between the photon energy ϵ and resonance. The spectra are shown *before* inclusion of lifetime broadening. The gray lines are the average of the two curves. The average is independent of \hat{e} for dipole transitions on a site with cubic symmetry. (The plot also reveals small zone-sampling artifacts.)

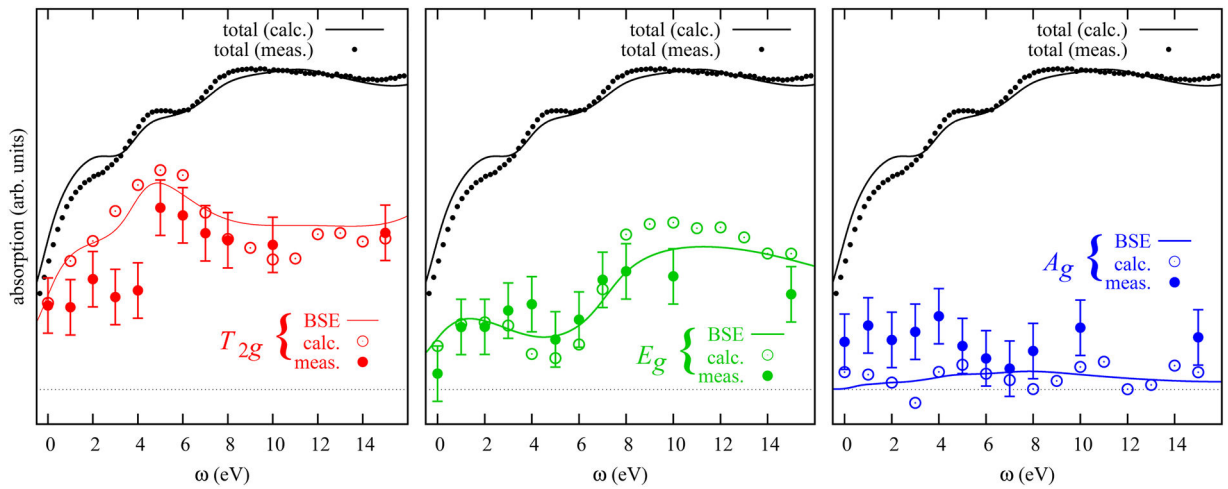


FIG. 10.

Partial or total $A_g L_3$ absorption spectra [the total being defined as $\epsilon_{2,L_3}(E_C + \omega)$].

The black curve and points common to all panels are the measured and calculated total absorption spectrum. For each symmetry ($X = T_{2g}$, E_g , and A_g), the lower solid curve is $\epsilon_{2,X}(E_C + \omega)$, defined in Eq. (8), deduced from BSE calculations. The hollow (filled) circles are the same quantity deduced from Eq. (8), but with the PDOS found by analyzing calculated (measured) $A_g L_3 - M_{4,5}M_{4,5}$ Auger spectra.